

Super-resolution of Sentinel-2 images: Learning a globally applicable deep neural network

Charis Lanaras^{a,*}, José Bioucas-Dias^b, Silvano Galliani^a, Emmanuel Baltsavias^a, Konrad Schindler^a

^a*Photogrammetry and Remote Sensing, ETH Zurich, Zurich, Switzerland*

^b*Instituto de Telecomunicações, Instituto Superior Técnico, Universidade de Lisboa, Portugal*

Abstract

The Sentinel-2 satellite mission delivers multi-spectral imagery with 13 spectral bands, acquired at three different spatial resolutions. The aim of this research is to super-resolve the lower-resolution (20 m and 60 m Ground Sampling Distance – GSD) bands to 10 m GSD, so as to obtain a complete data cube at the maximal sensor resolution. We employ a state-of-the-art convolutional neural network (CNN) to perform end-to-end upsampling, which is trained with data at lower resolution, *i.e.*, from 40→20 m, respectively 360→60 m GSD. In this way, one has access to a virtually infinite amount of training data, by downsampling real Sentinel-2 images. We use data sampled globally over a wide range of geographical locations, to obtain a network that generalises across different climate zones and land-cover types, and can super-resolve arbitrary Sentinel-2 images without the need of retraining. In quantitative evaluations (at lower scale, where ground truth is available), our network, which we call *DSen2*, outperforms the best competing approach by almost 50% in RMSE, while better preserving the spectral characteristics. It also delivers visually convincing results at the full 10 m GSD.

Keywords: Sentinel-2; super-resolution; sharpening of bands; convolutional neural network; deep learning

1. Introduction

Several widely used satellite imagers record multiple spectral bands with different spatial resolutions. Such instruments have the considerable advantage that the different spectral bands are recorded (quasi-) simultaneously, thus with similar illumination and atmospheric conditions, and without multi-temporal changes. Furthermore, the viewing directions are (almost) the same for all bands, and the co-registration between bands is typically very precise. Examples of such multi-spectral, multi-resolution sensors include: MODIS, VIIRS, ASTER, Worldview-3 and Sentinel-2. The resolutions between the spectral bands of any single instrument typically differ by a factor of about 2–6. Reasons for recording at varying spatial resolution include: storage and transmission bandwidth restrictions, improved signal-to-noise ratio (SNR) in some bands through larger pixels, and bands designed for specific purposes that do not require high spatial resolution (*e.g.* atmospheric corrections). Still, it is often desired to have all bands available at the highest spatial resolution, and the question arises whether it is possible to computationally super-resolve the

lower-resolution bands, so as to support more detailed and accurate information extraction. Such a high-quality super-resolution, beyond naive interpolation or pan-sharpening, is the topic of this paper. We focus specifically on super-resolution of Sentinel-2 images.

Sentinel-2 (S2) consists of two identical satellites, 2A and 2B, which use identical sensors and fly on the same orbit with a phase difference of 180 degrees, decreasing thus the repeat and revisit periods. The sensor acquires 13 spectral bands with 10 m, 20 m and 60 m resolution, with high spatial, spectral, radiometric and temporal resolution, compared to other, similar instruments. More details on the S2 mission and data are given in Section 3. Despite its recency, S2 data have been already extensively used. Beyond conventional thematic and land-cover mapping, the sensor characteristics also favour applications like hydrology and water resource management, or monitoring of dynamically changing geophysical variables.

E.g., Mura et al. (2018) exploit S2 to predict growing stock volume in forest ecosystems. Castillo et al. (2017) compute the Leaf Area Index (LAI) as a proxy for above-ground biomass of mangrove forests in the Philippines. Similarly, Clevers et al. (2017) retrieve LAI and leaf and canopy chlorophyll content of a potato crop. Delloye et al. (2018) estimate nitrogen uptake in intensive winter wheat cropping systems by retrieval of the canopy chlorophyll content. Paul et al. (2016) map the extent of glaciers, while Toming et al. (2016) map lake water quality. Immitzer et al. (2016) have demonstrated the use of S2 data for crop

*Corresponding author

Email addresses: charis.lanaras@geod.baug.ethz.ch
(Charis Lanaras), bioucas@lx.it.pt (José Bioucas-Dias), silvano.galliani@geod.baug.ethz.ch (Silvano Galliani), emmanuel.baltsavias@geod.baug.ethz.ch (Emmanuel Baltsavias), konrad.schindler@geod.baug.ethz.ch (Konrad Schindler)

and tree species classification, and Pesaresi et al. (2016) for detecting built-up areas. The quality, free availability and world-wide coverage make S2 an important tool for (current and) future earth observation, which motivates this work.

Obviously, low-resolution images can be upsampled with simple and fast, but naive methods like bilinear or bicubic interpolation. However, such methods return blurry images with little additional information content. More sophisticated methods, including ours, attempt to do better and recover as much as possible of the spatial detail, through a “smarter” upsampling that is informed by the available high-resolution bands. Here, we propose a (deep) machine learning approach to multi-spectral super-resolution, using convolutional neural networks (CNNs). The goal is to surpass the current state-of-the-art in terms of reconstruction accuracy, while at the same time to *preserve the spectral information* of the original bands. Moreover, the method shall be computationally efficient enough for large-area practical use. We train two CNNs, one for super-resolving 20 m bands to 10 m, and one for super-resolving 60 m bands to 10 m. Our method, termed DSen2, implicitly captures the statistics of all bands and their correlations, and jointly super-resolves the lower-resolution bands to 10 m GSD. See an example in Fig. 1. True to the statistical learning paradigm, we learn an end-to-end-mapping from raw S2 imagery to super-resolved bands purely from the statistics over a large amount of image data. Our approach is based on one main assumption, namely that the spectral correlation of the image texture is self-similar over a (limited) range of scales. *I.e.*, we postulate that upsampling from 20 m to 10 m GSD, by transferring high resolution (10 m) details across spectral bands, can be learned from ground truth images at 40 m and 20 m GSD; and similarly for the 60 m to 10 m case. Under this assumption, creating training data for supervised learning is simple and cheap: we only need to synthetically downsample original S2 images by the desired factor, use the downsampled version as input to generate original data as output.

In this way, one gains access to large amounts of training data, as required for deep learning: S2 data are available free of charge, covering all continents, climate zones, biomes and land-cover types. Moreover, we assert that the high-capacity of modern deep neural networks is sufficient to encode a super-resolution mapping which is valid across the globe. Fig. 2 and 3 show various land-cover types and geographical/climatic areas used for training and testing. It is likely that even better results could be achieved, if a user focusing on a specific task and geographic region re-trains the proposed networks with images from that particular environment. In that case, one can start from our trained network and fine-tune the network weights with appropriate training sites. However, our experiments show that even a single model, trained on a selected set of representative sites world-wide, achieves much better super-resolution than prior state-of-the-art methods for indepen-

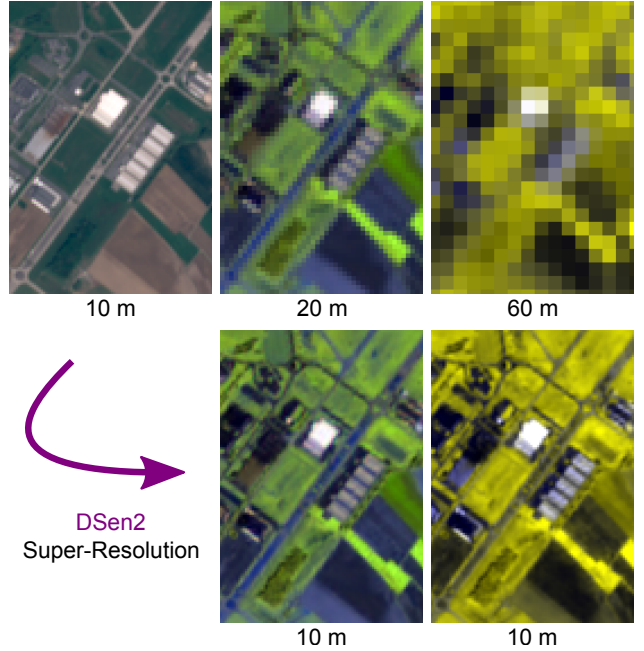


Figure 1: *Top:* Input Sentinel-2 bands at 10 m, 20 m and 60 m GSD, *Bottom:* Super-Resolved bands to 10 m GSD, with the proposed method (DSen2).

dent test sites, also sampled globally. That is, our network is not overfitted to a particular context (as often the case with discriminative statistical learning), but can be applied worldwide.

Extensive experimental tests at reduced scale (where S2 ground truth is available) show that our single, globally applicable network yields greatly improved super-resolution of all S2 bands to 10 m GSD. We compare our method to four other methods both quantitatively and qualitatively. Our approach achieves almost 50% lower RMSE than the best competing methods, as well as > 5 dB higher signal-to-reconstruction-error ratio and >30% improvement in spectral angle mapping. The performance difference is particularly pronounced for the Short-Wave Infrared (SWIR) bands and the 60 m ones, which are particularly challenging for super-resolution. For completeness, we also provide results for three “classical” pan-sharpening methods on the 20 m bands, which confirm that pan-sharpening cannot compete with true multi-band super-resolution methods, including ours. Importantly, we also train a version of our network at half resolution (80→40 m) and evaluate its performance on 40→20 m test data. While there is of course some loss in performance, the CNN trained in this way still performs significantly better than all other methods. This supports our assertion that the mapping is to a large extent scale-invariant and can be learned from training data at reduced resolution – which is important for machine learning approaches in general, beyond our specific implementation.

Summarising our contributions, we have developed a



Figure 2: A selection of the images used for training and testing.

CNN-based super-resolution algorithm optimised for (but conceptually not limited to) S2, with the following characteristics: (*i*) significantly higher accuracy of all super-resolved bands, (*ii*) better preservation of spectral characteristics, (*iii*) favourable computational speed when run on modern GPUs, (*iv*) global applicability for S2 data without retraining, according to our (necessarily limited) tests, (*v*) generic end-to-end system that can, if desired, be retrained for specific geographical locations and land-covers, simply by running additional training iterations, (*vi*) free, publicly available source code and pre-trained network weights, enabling out-of-the-box super-resolution of S2 data.

2. Related work

Enhancing the spatial resolution of remotely sensed multi-resolution images has been addressed for various types of images and sensors, including for example ASTER (Tonooka, 2005; Fasbender et al., 2008), MODIS (Trishchenko et al., 2006; Sirguey et al., 2008), and VIIRS (Picaro et al., 2016). In the following, we differentiate three types of methods: pan-sharpening per band, inverting an explicit imaging model, and machine learning approaches. The first group increases the spatial resolution independently for each target band, by blending in information from a spectrally overlapping high-resolution band. It is therefore essentially equivalent to classical pan-sharpening, applied separately to the spectral region around each high-resolution band. Such an approach relies on the assumption that for each relevant portion of the spectrum there is one high-resolution band (in classical pan-sharpening the “panchromatic” one), which overlaps, at least partially, with the lower-resolution bands to be enhanced. That view leads directly to the inverse problem of undoing the spatial blur from the panchromatic to the lower-resolution texture. A number of computational tools have been applied ranging from straight-forward *component substitution* to *multiresolution analysis*, *Bayesian inference* and *variational regularisation*. For a few representative examples we refer to (Choi et al., 2011), (Lee and Lee, 2010) and (Garzelli et al., 2008). A recent review and comparison of pan-sharpening methods can be found in Vivone et al. (2015). The pan-sharpening strategy has also been applied directly to Sentinel-2, although

the sensor does not meet the underlying assumptions: as opposed to a number of other earth observation satellites (e.g., Landsat 8) it does *not* have a panchromatic band that covers most of the sensor’s spectral range. In a comparative study Vaiopoulos and Karantzalos (2016) evaluate 21 pan-sharpening algorithms to enhance the 20m visible and near infrared (VNIR) and short wave infrared (SWIR) bands of Sentinel-2, using heuristics to select or synthesise the “panchromatic” input from the (in most cases non-overlapping) 10m bands. Wang et al. (2016) report some of the best results in the literature for their ATPRK (Area-To-Point Regression Kriging) method, which includes a similar band selection, performs regression analysis between bands at low resolution, and applies the estimated regression coefficients to the high-resolution input, with appropriate normalisation. Park et al. (2017) propose a number of modifications to optimise the band selection and synthesis, which is then used for pan-sharpening with component substitution and multiresolution analysis. Du et al. (2016), having in mind the monitoring of open water bodies, have tested four popular pan-sharpening methods to sharpen the B11 SWIR band of S2, in order to compute a high-resolution the normalized differential water index (NDWI). Further in this direction, Gasparovic and Jogun (2018) used five different pan-sharpening methods to enhance the resolution of the 20m bands. Their goal was to investigate the effect of the sharpened images on a land-cover classification compared to naive nearest neighbor up-sampling. Interestingly, the classification results improved for most of the methods.

The second group of methods attacks super-resolution as an inverse imaging problem under the variational, respectively Bayesian, inference frameworks. These *model-based* methods are conceptually appealing in that they put forward an explicit observation model, which describes the assumed blurring, downsampling, and noise processes. As the inverse problem is ill-posed by definition, they also add an explicit regulariser (in Bayesian terms an “image prior”). The high-resolution image is then obtained by minimising the residual error w.r.t. the model (respectively, the negative log-likelihood of the predicted image) in a single optimisation for all bands simultaneously. Brodu (2017) introduced a method that separates band-dependent spectral information from information that is common across all

Table 1: The 13 Sentinel-2 bands.

| Band | B1 | B2 | B3 | B4 | B5 | B6 | B7 | B8 | B8a | B9 | B10 | B11 | B12 |
|------------------------|-----|-----|-----|-----|-----|-----|-----|-----|-----|-----|------|------|------|
| Center wavelength [nm] | 443 | 490 | 560 | 665 | 705 | 740 | 783 | 842 | 865 | 945 | 1380 | 1610 | 2190 |
| Bandwidth [nm] | 20 | 65 | 35 | 30 | 15 | 15 | 20 | 115 | 20 | 20 | 30 | 90 | 180 |
| Spatial Resolution [m] | 60 | 10 | 10 | 10 | 20 | 20 | 20 | 10 | 20 | 60 | 60 | 20 | 20 |

bands, termed “geometry of scene elements”. The model then super-resolves the low-resolution bands such that they are consistent with those scene elements, while preserving their overall reflectance. [Lanaras et al. \(2017\)](#) adopt an observation model with per-band point spread functions that account for convolutional blur, downsampling, and noise. The regularisation consists of two parts, a dimensionality reduction that implies correlation between the bands, and thus lower intrinsic dimension of the signal; and a spatially varying, contrast-dependent penalisation of the (quadratic) gradients, which is learned from the 10 m bands. SMUSH, introduced in [Paris et al. \(2017\)](#), adopts an observation model similar to [Lanaras et al. \(2017\)](#), but employs a different, patch-based regularisation that promotes self-similarity of the images. The method proceeds hierarchically, first sharpening the 20 m bands, then the coarse 60 m ones.

The third group of super-resolution methods casts the prediction of the high-resolution data cube as a supervised *machine learning* problem. In contrast to the two previous groups, the relation between lower-resolution input to higher-resolution output is not explicitly specified, but learned from example data. Learning methods (and in particular, deep neural networks) can thus capture much more complex and general relations, but in turn require massive amounts of training data, and large computational resources to solve the underlying, extremely high-dimensional and complex optimisation. We note that the methods described in the following were designed with the classic pan-sharpening problem in mind. Due to the generic nature of end-to-end machine learning, this does not constitute a conceptual problem: in principle, they could be re-trained with different input and output dimensions. Obviously, their current weights are not suitable for Sentinel-2 upsampling. To the best of our knowledge, we are the first to apply deep learning to that problem. [Masi et al. \(2016\)](#) adapt a comparatively shallow three-layer CNN architecture originally designed for single-image (blind) super-resolution. They train pan-sharpening networks for Ikonos, GeoEye-1 and WorldView-2. [Yang et al. \(2017\)](#) introduced PanNet, based on the high-performance ResNet architecture ([He et al., 2016](#)). PanNet starts by upsampling the low-resolution inputs with naive interpolation. The actual network is fed with high-pass filtered versions of the raw inputs and learns a correction that is added to the naively upsampled images.¹ PanNet was trained for Worldview-

2, WorldView-3, and Ikonos. More recently, this concept has been further exploited in [Scarpa et al. \(2018\)](#). Learning based pan-sharpening networks are trained with relatively small amounts of data, presumably because of the high data cost. In this context, we point out that with deep learning one need not specify sensor characteristics like for instance spectral response functions. Rather, the sensor properties are implicit in the training data.

Example-based super-resolution has been investigated in computer vision and image processing (e.g., [Freeman et al., 2002](#)), but mainly for single-image super-resolution. *I.e.*, enhancing the spatial resolution of a single (RGB) image with the help of a prior learned from a suitable training set. The rise of deep learning has also advanced single-image super-resolution ([Lim et al., 2017](#); [Kim et al., 2016](#)). Moreover, such super-resolution has been applied to Sentinel-2 and Landsat-8 images ([Pouliot et al., 2018](#)). All these works have in common that they *predict* images of higher spatial resolution, meaning that what is learned is a generic prior on the local structure of high-resolution images; whereas our method increases resolution of particular bands in a more informed and more accurate manner, by *transferring* the texture from available high-resolution bands; effectively learning a prior on the correlations across the spectrum (or, equivalently, on the high-resolution structure of some bands *conditioned* on the known high-resolution structure of other bands).

3. Input data

We use data from the ESA/Copernicus satellites Sentinel 2A and 2B². They were launched on June 23, 2015 and March 7, 2017, respectively, with a design lifetime of 7.25 years, potentially extendible up to 5 additional years. The two satellites are identical and have the same sun-synchronous, quasi-circular, near-polar, low-earth orbit with a phase difference of 180 degrees. This allows the reduction of the repeat (and revisit) periods from 10 to 5 days at the equator. The satellites systematically cover all land masses except Antarctica, including all major and some smaller islands. The main sensor on the satellites is a multispectral imager with 13 bands. Their spectral characteristics and GSDs are shown in Table 1. Applications of the

¹In CNN terminology, adding the upsampled input constitutes a “skip connection”.

²See details at <https://eoportal.org/web/eoportal/satellite-missions/c-missions/copernicus-sentinel-2>

10 m and 20 m bands include: general land-cover mapping, agriculture, forestry, mapping of biophysical variables (for instance, leaf chlorophyll content, leaf water content, leaf area index), monitoring of coastal and inland waters, and risk and disaster mapping. The three bands with 60 m GSD are intended mainly for water vapour, aerosol corrections and cirrus clouds estimation. In actual fact they are captured at 20 m GSD and are downsampled in software to 60 m, thus increasing the SNR. The first 10 bands cover the VNIR spectrum and are acquired by a CMOS detector for two bands (B3 and B4) with 2-line TDI (time delay and integration) for better signal quality. The last 3 bands cover the SWIR spectrum and are acquired by passively cooled HgCdTe detectors. Bands B11 and B12 also have staggered-row, 2-line TDI. The swath width is 290 km. Intensities are quantised to 12 bit and compressed by a factor ≈ 2.9 with a lossy wavelet method (depending on the band). Empirical data quality has been quantified as: absolute geolocation accuracy (without ground control) of 11 m at 95.5% confidence, absolute radiometric uncertainty (except B10) $< 5\%$, and SNR values comply to the specifications with $> 27\%$ margin.

Clerc and MPC Team (2018) report on further aspects of S2 data quality. The mean pairwise co-registration errors between spectral bands are 0.14–0.21 pixels (at the lower of the two resolutions) for S2A and 0.07–0.18 pixels for S2B, 99.7% confidence. This parameter is important for our application: good band-to-band co-registration is important for super-resolution, and S2 errors are low enough to ignore them and proceed without correcting band-to-band offsets. Moreover, data quality is very similar for Sentinel-2A and 2B, so that no separate treatment is required. B10 (in an atmospheric absorption window, included for cirrus clouds detection) has comparatively poor radiometric quality and exhibits across-track striping artifacts, and is excluded from many aspects of quality control. For that reason we also exclude it.

Potential sensor issues that could impair super-resolution would mainly be band-to-band misregistration (which is very low for S2), radiometric or geometric misalignments within a band (which do not seem to occur), and moving objects such as airplanes (which are very rare). The data thus fulfills the preconditions for super-resolution, and we did not notice any effects in our results that we attribute to sensor anomalies.

S2 data can be downloaded from the Copernicus Services Data Hub, free of charge. The data comes in tiles (granules) of $110 \times 110 \text{ km}^2$ ($\approx 800\text{MB}$ per tile). For processing, we use the Level-1C top-of-atmosphere (TOA) reflectance product, which includes the usual radiometric and geometric corrections. The images are geocoded and orthorectified using the 90m DEM grid (PlanetDEM³) with a height (LE95) and planimetric (CE95) accuracy of 14 m

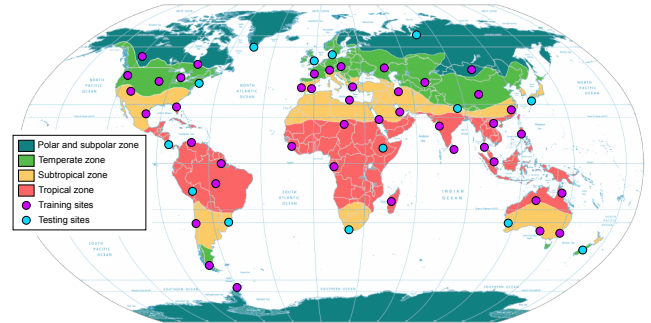


Figure 3: Locations of Sentinel-2 tiles used for training and testing. Image source: meteoblue.com

and 10 m, respectively. We note that a refinement step for the Level-1C processing chain is planned, which shall bring the geocoding accuracy between different passes to < 0.3 pixels at 95% confidence, which will allow high-accuracy multi-temporal analysis.

In this study, we use data from both Sentinel 2A and 2B, acquired between December 2016 and November 2017, respectively July 2017 and November 2017. Fig. 3 shows the locations of the tiles used. They have been picked randomly, aiming for a roughly even distribution on the globe and for variety in terms of climate zone, land-cover and biome type. To simplify implementation and testing, we chose only tiles with no undefined (“black background”) pixels. Pointers to the exact tiles are included in our publicly available implementation (see below). Using this wide variety of scenes, we aim to train a globally applicable super-resolution network that can be applied to any S2 scene.

4. Method

We adopt a deep learning approach to Sentinel-2 super-resolution. The rationale is that the relation between the multi-resolution input and a uniform, high-resolution output data cube is a complex mixture of correlations across many (perhaps all) spectral bands, over a potentially large spatial context, respectively texture neighbourhood. It is thus not obvious how to design a suitable prior (regulariser) for the mapping. On the contrary, the underlying statistics can be assumed to be the same across different Sentinel-2 images. We therefore use a CNN to directly learn it from data. In other words, the network serves as a big regression engine from raw multi-resolution input patches to high-resolution patches of the bands that need to be upsampled. We found that it is sufficient to train two separate networks for the 20 m and 60 m bands. *I.e.*, the 60 m resolution bands, unsurprisingly, do not contribute information to the upsampling from 20 to 10 m.

We point out that the machine learning approach is generic, and not limited to a specific sensor. For our application the network is specifically tailored to the image

³<https://www.planetobserver.com/products/planetdem/planetdem-30/>

statistics of Sentinel-2. But the sensor-specific information is encoded only in the network weights, so it can be readily retrained for a different multi-resolution sensor.

4.1. Simulation process

CNNs are fully supervised and need (a lot of) training data, *i.e.*, patches for which both the multi-resolution input and the true high-resolution output are known. Thus, a central issue in our approach is how to construct the training, validation and testing datasets, given that ground truth with 10 m resolution is not available for the 20 m and 60 m bands. Even with great effort, *e.g.*, using aerial hyperspectral data and sophisticated simulation technology, it is at present impossible to synthesise such data with the degree of realism necessary for faithful super-resolution. Hence, to become practically viable, our approach therefore requires one fundamental assumption: we posit that the transfer of spatial detail from high-resolution to low-resolution bands is scale-invariant and that it depends only on the relative resolution difference, but not on the absolute GSD of the images. *I.e.* the relations between bands of different resolutions are *self-similar* within the relevant scale range. Note however, we require only a weak form of self-similarity: it is not necessary for our network to learn a “blind” generative mapping from lower to higher resolution. Rather, it only needs to learn how to transfer high frequency details from existing high-resolution bands. The literature on self-similarity in image analysis supports such an assumption (*e.g.*, Shechtman and Irani, 2007; Glasner et al., 2009), at least over a certain scale range. We emphasise that for our case, the assumption must hold only over a limited range up to $6\times$ resolution differences, *i.e.*, less than one order of magnitude. In this way, virtually unlimited amounts of training data can be generated by synthetically downsampling raw Sentinel-2 images as required.

For our purposes, the scale-invariance means that the mappings between, say, 20 \rightarrow 10 m and 40 \rightarrow 20 m are roughly equivalent. We can therefore train our CNN on the latter and apply it to the former. If the assumed invariance holds, the learned spatial-spectral correlations will be correct. To generate training data with a desired scale ratio s , we downsample the original S2 data, by first blurring it with a Gaussian filter of standard deviation $\sigma = 1/s$ pixels, emulating the modulation transfer function (*mtf*) of S2. From the Data Quality Report (Clerc and MPC Team, 2018) we get a range of 0.44–0.55 for the point spread function (*psf*) of the bands, given the relation $psf = \sqrt{-2 \log(mtf)/\pi^2}$. Then we downsample by averaging over $s \times s$ windows, with $s = 2$ respectively $s = 6$. The process of generating the training data is schematised in Fig. 4. In this way, we obtain two datasets for training, validation and testing. The first dataset consists of “high-resolution” images at 20 m GSD and “low-resolution” images of 40 m GSD, created by downsampling the original 10 m and 20 m bands by a factor of 2. It serves to train a network for $2\times$ super-resolution. The second one consists of images with 60 m, 120 m and

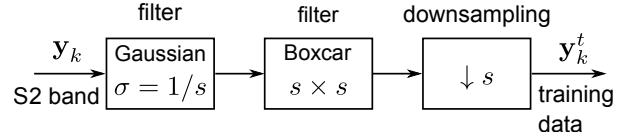


Figure 4: The downsampling process used for simulating the data for training and testing.

360 m GSD, downsampled from the original 10 m, 20 m and 60 m data. This dataset is used to learn a network for $6\times$ super-resolution. We note that, due to unavailability of 10 m ground truth, quantitative analysis of the results must also be conducted at the reduced resolution. We chose the following strategy: to validate the self-similarity assumption, we train a network at quarter-resolution 80 \rightarrow 40 m as well as one at half-resolution 40 \rightarrow 20 m and verify that both achieve satisfactory performance on the ground truth 20 m images. To test the actual application scenario, we then apply the 40 \rightarrow 20 m network to real S2 data to get 20 \rightarrow 10 m super-resolution. However, the resulting 10 m super-resolved bands can only be checked by visual inspection.

4.2. 20m and 60m resolution networks

To avoid confusion between bands and simplify notation, we collect bands that share the same GSD into three sets $A = \{B_2, B_3, B_4, B_8\}$ (GSD=10 m), $B = \{B_5, B_6, B_7, B_{8a}, B_{11}, B_{12}\}$ (GSD=20 m) and $C = \{B_1, B_9\}$ (GSD=60 m). The spatial dimensions of the high-resolution bands in A are $W \times H$. Further, let $\mathbf{y}_A \in \mathbb{R}^{W \times H \times 4}$, $\mathbf{y}_B \in \mathbb{R}^{W/2 \times H/2 \times 6}$, and $\mathbf{y}_C \in \mathbb{R}^{W/6 \times H/6 \times 2}$ denote, respectively, the observed intensities of all bands contained in sets A , B and C . As mentioned above, we train two separate networks for different super-resolution factors. This reflects our belief that self-similarity may progressively degrade with increasing scale difference, such that 120 \rightarrow 60 m is probably a worse proxy for 20 \rightarrow 10 m than the less distant 40 \rightarrow 20 m.

The first network upsamples the bands in B using information from A and B :

$$\mathcal{T}_{2\times} : \mathbb{R}^{W \times H \times 4} \times \mathbb{R}^{W/2 \times H/2 \times 6} \rightarrow \mathbb{R}^{W \times H \times 6} \quad (1a)$$

$$(\mathbf{y}_A, \mathbf{y}_B) \mapsto \mathbf{x}_B, \quad (1b)$$

where $\mathbf{x}_B \in \mathbb{R}^{W \times H \times 6}$ denotes the super-resolved 6-band image with GSD 10 m. The second network upsamples C , using information from A , B and C :

$$\begin{aligned} \mathcal{S}_{6\times} : & \mathbb{R}^{W \times H \times 4} \times \mathbb{R}^{W/2 \times H/2 \times 6} \times \mathbb{R}^{W/6 \times H/6 \times 2} \\ & \rightarrow \mathbb{R}^{W \times H \times 2} \end{aligned} \quad (2a)$$

$$(\mathbf{y}_A, \mathbf{y}_B, \mathbf{y}_C) \mapsto \mathbf{x}_C, \quad (2b)$$

with $\mathbf{x}_C \in \mathbb{R}^{W \times H \times 2}$ again the super-resolved 2-band image of GSD 10 m.

4.3. Basic architecture

Our network design was inspired by EDSR (Lim et al., 2017), state-of-the-art in single-image super-resolution. EDSR follows the well-known ResNet architecture (He et al., 2016) for image classification, which enables the use of very deep networks by using the so called “skip connections”. These long-range connections bypass portions of the network and are added again later, such that skipped layers only need to estimate the residual w.r.t. their input state. In this way the average effective path length through the network is reduced, which alleviates the vanishing gradient problem and greatly accelerates the learning.

Our problem however, is different from classical single-image super-resolution. In the case of Sentinel-2, the network does not need to hallucinate the high-resolution texture only on the basis of previously seen images. Rather, it has access to the high-resolution bands to guide the super-resolution, *i.e.*, it must learn to *transfer* the high-frequency content to the low-resolution input bands, and do so in such a way that the resulting (high-resolution) pixels have plausible spectra. Contrary to EDSR, where the upsampling takes place at the end, we prefer to work with the high (10 m) resolution from the beginning, since some input bands already have that resolution. We thus start by up-sampling the low-resolution bands \mathbf{y}_B and \mathbf{y}_C to the target resolution (10 m) with simple bilinear interpolation, to obtain $\tilde{\mathbf{y}}_B \in \mathbb{R}^{W \times H \times 6}$ and $\tilde{\mathbf{y}}_C \in \mathbb{R}^{W \times H \times 2}$. The inputs and outputs depend on whether the network $\mathcal{T}_{2\times}$ or $\mathcal{S}_{6\times}$ is used. To avoid confusion we define the set k of low-resolution bands as either $k = \{B\}$ or $k = \{B, C\}$. Such that the input is \mathbf{y}_k , and the addition (skip connection) to the output is $\tilde{\mathbf{y}}_B$ for $\mathcal{T}_{2\times}$, respectively $\tilde{\mathbf{y}}_C$ for $\mathcal{S}_{6\times}$. The proposed network architecture consists mainly of convolutional layers, *ReLU* non-linearities and skip connections. A graphical overview of the network is given in Fig. 5 and 6, pseudo-code for the network specification is given in Algorithm 1.

The operator $\text{conv}(\mathbf{x}, f_{out})$ represents a single convolution layer, *i.e.*, a multi-dimensional convolution of image \mathbf{z} with kernel \mathbf{w} , followed by an additive bias \mathbf{b} :

$$\mathbf{v} = \text{conv}(\mathbf{x}, f_{out}) := \mathbf{w} * \mathbf{z} + \mathbf{b} \quad (3)$$

$$\mathbf{w} : (f_{out} \times f_{in} \times k \times k), \mathbf{b} : (f_{out} \times 1 \times 1 \times 1)$$

$$\mathbf{z} : (f_{in} \times w \times h), \mathbf{v} : (f_{out} \times w \times h)$$

where $*$ is the convolution operator. The convolved image \mathbf{v} has the same spatial dimensions ($w \times h$) as the input, as we use zero-padded convolution. The convolution kernels \mathbf{w} have dimensions $(k \times k)$. We always use $k = 3$, in line with the recent literature, which suggests that many layers of small kernels are preferable. The output feature dimension f_{out} of the convolution (number of filters) depends only on \mathbf{w} and is required as an input. f_{out} can be chosen for each convolutional layer, and constitutes a hyper-parameter of the network. Its selection is further discussed in Sec. 4.4. The input feature dimensions f_{in} (depth of the filters) depend only on the input image \mathbf{z} . The weights \mathbf{w}

Algorithm 1 DSen2. Network architecture.

Require: high-resolution bands (A): \mathbf{y}_A , low-resolution bands (B, C): \mathbf{y}_k , feature dimensions f , number of ResBlocks: d

Cubic interpolation of low resolution:
 Upsample \mathbf{y}_k to $\tilde{\mathbf{y}}_k$

Concatenation:
 $\mathbf{x}_0 := [\mathbf{y}_A, \tilde{\mathbf{y}}_k]$

First Convolution and ReLU:
 $\mathbf{x}_1 := \max(\text{conv}(\mathbf{x}_0, f), 0)$

Repeat the ResBlock module d times:
for $i = 1$ **to** d **do**

$\mathbf{x}_i = \text{ResBlock}(\mathbf{x}_{i-1}, f)$

end for

Last Convolution to match the output dimensions:
where b_{last} is either 6 ($\mathcal{T}_{2\times}$) or 2 ($\mathcal{S}_{6\times}$)

$\mathbf{x}_{d+1} := \text{conv}(\mathbf{x}_d, b_{last})$

Skip connection:
 $\mathbf{x} := \mathbf{x}_{d+1} + \tilde{\mathbf{y}}_B \ (\mathcal{T}_{2\times}) \quad \text{or} \quad \mathbf{x} := \mathbf{x}_{d+1} + \tilde{\mathbf{y}}_C \ (\mathcal{S}_{6\times})$

return \mathbf{x}

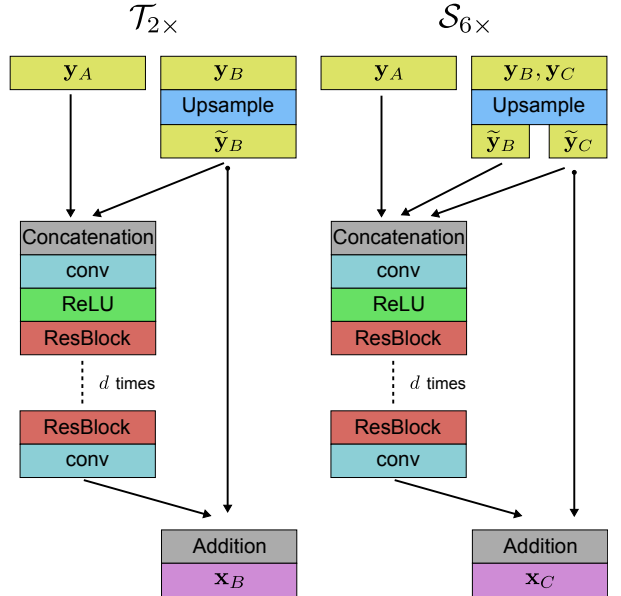


Figure 5: The proposed networks $\mathcal{T}_{2\times}$ and $\mathcal{S}_{6\times}$, with multiple ResBlock modules. The two networks differ only regarding the inputs.

and \mathbf{b} are the free parameters learned during training and ultimately what the network has to learn.

The rectified linear unit (*ReLU*) is a simple non-linear function that truncates all negative responses in the output to 0:

$$\mathbf{v} = \max(\mathbf{z}, 0). \quad (4)$$

A residual block $\mathbf{v} = \text{ResBlock}(\mathbf{z}, f)$ is defined as a series of layers that operate on an input image \mathbf{z} to generate an

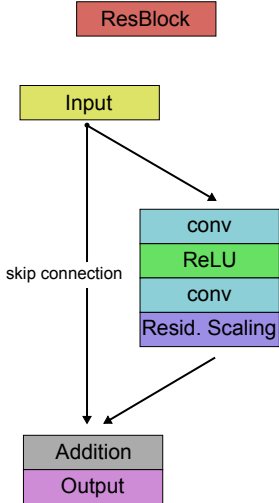


Figure 6: Expanded view of the Residual Block.

output \mathbf{z}_4 , then adds that output to the input image (Fig. 6):

$$\begin{aligned} \mathbf{z}_1 &= \text{conv}(\mathbf{z}, f) && \# \text{convolution} && (5a) \\ \mathbf{z}_2 &= \max(\mathbf{z}_1, 0) && \# \text{ReLU layer} && (5b) \\ \mathbf{z}_3 &= \text{conv}(\mathbf{z}_2, f) && \# \text{convolution} && (5c) \\ \mathbf{z}_4 &= \lambda \cdot \mathbf{z}_3 && \# \text{residual scaling} && (5d) \\ \mathbf{v} &= \mathbf{z}_4 + \mathbf{z} && \# \text{skip connection} && (5e) \end{aligned}$$

λ is a custom layer (5d) that multiplies its input activations (multi-dimensional images) with a constant. This is also termed *residual scaling* and greatly speeds up the training of very deep networks (Szegedy et al., 2017). In our experience residual scaling is crucial and we always use $\lambda = 0.1$. As an alternative, we also tested the more common Batch Normalization (BN), but found that it did not improve accuracy or training time, while increasing the parameters of the network. Also, Lim et al. (2017) report that BN normalises the features and thus reduces the range flexibility (the actual reflectance) of the images. Within each ResBlock module we only include a *ReLU* after the first convolution, but not after the second, since our network shall learn corrections to the bilinearly upsampled image, which can be negative. Within our network design, the ResBlock module can be repeated as often as desired. We show experiments with two different numbers d of ResBlocks: 6 and 32. The final convolution at the head of the network, after all ResBlocks, reduces the output dimension to b_{last} , such that it matches the number of the required output bands (\mathbf{x}_B and \mathbf{x}_C). So $f_{out} = b_{last} = 6$ for $\mathcal{T}_{2\times}$, and $f_{out} = b_{last} = 2$ for $\mathcal{S}_{6\times}$ is used.

A particularity of our network architecture is a long, additive *skip connection* directly from the rescaled input to the output (Fig. 5). This means that the complete network in fact learns the additive correction from the bilinearly upsampled image to the desired output. The strategy to predict the differences from a simple, robust bilinear interpolation,

rather than the final output image, helps to preserve the radiometry of the input image.

4.4. Deep and very deep networks

Finding the right size and capacity for a CNN is largely an empirical choice. Conveniently, the CNN framework makes it possible to explore a range of depths with the same network design, thus providing an easy way of exploring the trade-off between small, efficient models and larger, more powerful ones. Also in our case, it is hard to know in advance how complex the network must be to adequately encode the super-resolution mapping. We introduce two configurations of our ResNet architecture, a deep (DSen2) and a very deep one (VDSen2). The names are derived from *Deep Sentinel-2* and *Very Deep Sentinel-2*, respectively. For the deep version we use $d = 6$ and $f = 128$, corresponding to 14 convolutional layers, respectively 1.8 million tunable weights. For the very deep one we set $d = 32$ and $f = 256$, leading to 66 convolutional layers and a total of 37.8 million tunable weights. DSen2 is comparatively small for a modern CNN. The design goal here was a light network that is fast in training and prediction, but still reaches good accuracy. VDSen2 has a lot higher capacity, and was designed with maximum accuracy in mind. It is closer in terms of size and training time to modern high-end CNNs for other image analysis tasks (Simonyan and Zisserman, 2015; He et al., 2016; Huang et al., 2017), but is approximately two times slower and five times slower in both training and prediction respectively, compared to its shallower counterpart (DSen2). Naturally, one can easily construct intermediate versions by changing the corresponding parameters d and f . The optimal choice will depend on the application task as well as available computational resources. On the one hand, the very deep variant is consistently a bit better, while training and applying it is not more difficult, if adequate resources (*i.e.*, high-end GPUs) are available. However, the gains are small compared to the $20\times$ increase in free parameters, and it is unlikely that going even deeper will bring much further improvement.

4.5. Training details

As loss function we use the mean absolute pixel error (L^1 norm) between the true and the predicted high-resolution image. Interestingly, we found the L^1 norm to converge faster and deliver better results than the L^2 norm, even though the latter serves as error metric during evaluation. Most likely this is due to the L^1 norm's greater robustness of absolute deviations to outliers. We did observe that some Sentinel-2 images contain a small number of pixels with very high reflectance, and due to the high dynamic range these reach extreme values without saturating.

Our learning procedure is standard: the network weights are initialised to small random values with the *HeUniform* method (He et al., 2015), and optimised with stochastic gradient descent (where each gradient step consists of a forward pass to compute the current loss over a small random

batch of image patches, followed by back-propagation of the error signal through the network). In detail, we use the Adam variant of SGD (Kingma and Ba, 2014) with Nesterov momentum (Dozat, 2015). Empirically, the proposed network architecture converges faster than other ones we experimented with, due to the ResNet-style skip connections.

Sentinel-2 images are too big to fit them into GPU memory for training and testing, and in fact it is unlikely that long-range context over distances of a kilometer or more plays any significant role for super-resolution at the 10 m level. With this in mind, we train the network on small patches of $w \times h = (32 \times 32)$ for $\mathcal{T}_{2\times}$, respectively (96×96) pixels for $\mathcal{S}_{6\times}$. We note that this corresponds to a receptive field of several hundred metres on the ground, sufficient to capture the local low-level texture and potentially also small semantic structures such as individual buildings or small waterbodies, but not large-scale topographic features. We do not expect the latter to hold much information about the local pixel values, instead there is a certain danger that the large-scale layout of a limited training set it is too unique to generalise to unseen locations.

As our network is *fully convolutional*, it can process input images of arbitrary spatial extent $w \times h$ (after padding to a multiple of the patch size). The tile size in the prediction step is limited only by the on-board memory on the GPU. To avoid boundary artifacts from tiling, adjacent tiles are cropped with an overlap of 2 low-resolution input pixels, corresponding to 40 m for $\mathcal{T}_{2\times}$, respectively 120 m for $\mathcal{S}_{6\times}$.

5. Experimental results

5.1. Implementation details

As mentioned before, we aim for global coverage. We therefore sample 60 representative scenes from around the globe, 45 for training and 15 for testing. For $\mathcal{T}_{2\times}$ we sample 8000 random patches per training image, for a total of 360,000 patches. For $\mathcal{S}_{6\times}$, we sample 500 patches per image for a total of 22,500 (note that each patch covers a 9 \times larger area in object space and has 9 \times more high-resolution pixels than for $\mathcal{T}_{2\times}$). Out of these patches 90% are used for training the weights, the remaining 10% serve as validation set, see Table 2. To test the networks, we run both on the 15 test images, each with a size of 110 \times 110 km 2 , which corresponds to 5,490 \times 5,490 pixels at 20 m GSD, or 1,830 \times 1,830 pixels at 60 m GSD.

Each network is implemented in the Keras framework (Chollet et al., 2015), with TensorFlow as back-end. Training is run on a NVIDIA Titan Xp GPU, with 12 GB of RAM, for approximately 3 days. The mini-batch size for SGD is set to 128 to fit into GPU memory. The initial learning rate is $lr = 1e-4$ and it is reduced by a factor of 2 whenever the validation loss does not decrease for 5 consecutive epochs. For numerical stability we divide the raw 0 – 10,000 reflectance values by 2000 before processing.

Table 2: Training and testing split.

| | Images | Split | Patches |
|-------------------------|--------|------------|---------------------------|
| $\mathcal{T}_{2\times}$ | 45 | Training | 90% $324,000 \times 32^2$ |
| | | Validation | 10% $36,000 \times 32^2$ |
| | 15 | Test | $15 \times 5,490^2$ |
| $\mathcal{S}_{6\times}$ | 45 | Training | 90% $20,250 \times 96^2$ |
| | | Validation | 10% $2,250 \times 96^2$ |
| | 15 | Test | $15 \times 1,830^2$ |

5.2. Baselines and evaluation metrics

As baselines, we use the methods of Lanaras et al. (2017) – termed SupReME, Wang et al. (2016) – termed ATPRK, and Brodu (2017) – termed Superres. Moreover, as elementary baseline we use bicubic interpolation, to illustrate naive upsampling without considering spectral correlations. Note, this also directly shows the effect of our network, which is trained to refine a bilinearly upsampled image. The input image sizes for the baselines were chosen to obtain the best possible results. SupReME showed the best performance when run with patches of 256, respectively 240 for $\mathcal{T}_{2\times}$ and $\mathcal{S}_{6\times}$. We speculate that this may be due to the subspace projection used within SupReME, which can better adapt to the local image content with moderate tile size. The remaining baselines performed best on full images. The parameters for all baselines were set as suggested in the original publications. This lead to rather consistent results across the test set.

The main evaluation metric of our quantitative comparison is the root mean squared error (RMSE), estimated independently per spectral band:

$$\text{RMSE} = \sqrt{\frac{1}{n} \sum (\hat{\mathbf{x}} - \mathbf{x})^2}, \quad (6)$$

where $\hat{\mathbf{x}}$ is each reconstructed band (vectorised), \mathbf{x} is the vectorised ground truth band and n the number of pixels in \mathbf{x} . The unit of the Sentinel-2 images is reflectance multiplied by 10,000, however, some pixels on specularities, clouds, snow etc. exceed 10,000. Therefore, we did not apply any kind of normalisation, and report RMSE values in the original files' value range, meaning that a residual of 1 corresponds to a reflectance error of 10^{-4} .

Depending on the scene content, some images have higher reflectance values than others, and typically also higher absolute reflectance errors. To compensate for this effect, we also compute the *signal to reconstruction error ratio* (SRE) as additional error metric, which measures the error relative to the power of the signal. It is computed as:

$$\text{SRE} = 10 \log_{10} \frac{\mu_{\mathbf{x}}^2}{\|\hat{\mathbf{x}} - \mathbf{x}\|^2/n}, \quad (7)$$

where $\mu_{\mathbf{x}}$ is the average value of \mathbf{x} . The values of SRE are given in decibels (dB). We point out that using SRE,

which measures errors relative to the mean image intensity, is better suited to make errors comparable between images of varying brightness. Whereas the popular peak signal to noise ratio (PSNR) would not achieve the same effect, since the peak intensity is constant. Moreover, we also compute the spectral angle mapper (SAM), *i.e.*, the angular deviation between true and estimated spectral signatures (Yuhas et al., 1992). We compute the SAM for each pixel and then average over the whole image. The values of SAM are given in degrees. This metric is complimentary to the two previous ones, and quite useful for some applications, in that it measures how faithful the relative spectral distribution of a pixel is reconstructed, while ignoring absolute brightness. Finally, we report the universal image quality index (UIQ) (Wang and Bovik, 2002). This metric evaluates the reconstructed image in terms of luminance, contrast, and structure. UIQ is unitless and its maximum value is 1.

5.3. Evaluation at lower scale

Quantitative evaluation on Sentinel-2 images is only possible at the lower scale at which the models are trained. *I.e.*, $\mathcal{T}_{2\times}$ is evaluated on the task to super-resolve 40→20 m, where the 40 m low-resolution and 20 m high-resolution bands are generated by synthetically degrading the original data – for details see Sec. 4.1. In the same way, $\mathcal{S}_{6\times}$ is evaluated on the super-resolution task from 360→60 m. Furthermore, to support the claim that the upsampling function is to a sufficient degree scale-invariant, we also run a test where we train $\mathcal{T}_{2\times}$ on the upsampling task from 80→40 m, and then test that network to the 40→20 m upsampling task. In the following, we separately discuss the $\mathcal{T}_{2\times}$ and $\mathcal{S}_{6\times}$ networks.

$\mathcal{T}_{2\times} - 20\text{m bands}$. We start with results for the $\mathcal{T}_{2\times}$ network, trained for super-resolution of actual S2 data to 10 m. Average results over all 15 test images and all bands in $B = \{\text{B5}, \text{B6}, \text{B7}, \text{B8a}, \text{B11}, \text{B12}\}$ are displayed in Table 3. The state-of-the-art methods SupReME and Superres perform similar, with Superres slightly better in all error metrics. DSen2 reduces the RMSE by 48% compared to the previous state-of-the-art. The other error measures confirm this gulf in performance (>5 dB higher SRE, 24% lower SAM). VDSen2 further improves the results, consistently over all error measures (except UIQ, where their scores are exactly the same). Relative to the leap from the best baseline to DSen2 the differences may seem small, but note that 0.3 dB would still be considered a marked improvement in many image enhancement tasks. Interestingly, ATPRK and SupReME yield rather poor results for SAM (relative spectral fidelity). Among the baselines, only Superres beats bicubic upsampling. Our method again wins comfortably, more than doubling the margin between the strongest competitor Superres and the simplistic baseline of bicubic upsampling.

Table 3: Aggregate results for $2\times$ upsampling of the bands in set B , evaluated at lower scale (input 40 m, output 20 m). Best results in bold.

| Training | RMSE | SRE | SAM | UIQ |
|---------------|-------|-------------|-------------|-------------|
| Bicubic | 123.5 | 25.3 | 1.24 | 0.821 |
| ATPRK | 116.2 | 25.7 | 1.68 | 0.855 |
| SupReME | 69.7 | 29.7 | 1.26 | 0.887 |
| Superres | 66.2 | 30.4 | 1.02 | 0.915 |
| DSen2 (ours) | 40→20 | 34.5 | 36.0 | 0.78 |
| VDSen2 (ours) | 40→20 | 33.7 | 36.3 | 0.76 |
| DSen2 (ours) | 80→40 | 51.7 | 32.6 | 0.89 |
| VDSen2 (ours) | 80→40 | 51.6 | 32.7 | 0.88 |
| | | | | 0.925 |

In the second test, we train an auxiliary $\mathcal{T}_{2\times}$ network on 80→40 m instead of the 40→20 m, but nevertheless evaluate it on the 20 m ground truth (while the model has never seen a 20 m GSD image). Of course this causes some drop in performance, but the performance stays well above all baselines, across all bands. *I.e.*, the learned mapping is indeed sufficiently scale-invariant to beat state-of-the-art model-based approaches, which by construction should not depend on the absolute scale. For our actual setting, train on 40→20 m then use for 20→10 m, one would expect even a smaller performance drop (compared to train on 80→40 m then use for 40→20 m), because of the well-documented inverse relation between spatial frequency and contrast in image signals (e.g., Ruderman, 1994; van der Schaaf and van Hateren, 1996; Srivastava et al., 2003). This experiment justifies our assumption, at $2\times$ reduced resolution, that training 40→20 m super-resolution on synthetically degraded images is a reasonable proxy for the actual 20→10 m upsampling of real Sentinel-2 images. We note that this result has potential implications beyond our specific CNN approach. It validates the general procedure to train on lower-resolution imagery, that has been synthesised from the original sensor data. That procedure is in no way specific to our technical implementation, and in all likelihood also not to the sensor characteristics of Sentinel-2.

Tables 4 and Fig. 7 show detailed per-band results. The large advantage for our method is consistent across all bands, and in fact particularly pronounced for the challenging extrapolation to B11 and B12. We point out that the RMSE values for B6, B7 and B8a are higher than for the other bands (with all methods). In these bands also the reflectance is higher. The relative errors, as measured by SRE, are very similar. Among our two networks, VDSen2 holds a moderate, but consistent benefit over its shallower counterpart across all bands, in both RMSE and SRE. In terms of UIQ, they both rank well above the competition, but there is no clear winner. We attribute this to limitations of the UIQ metric, which is a product of three terms and thus not overly stable near its maximum of 1.

It is interesting to note that the baselines exhibit a marked drop in accuracy for bands B11 and B12, whereas our net-

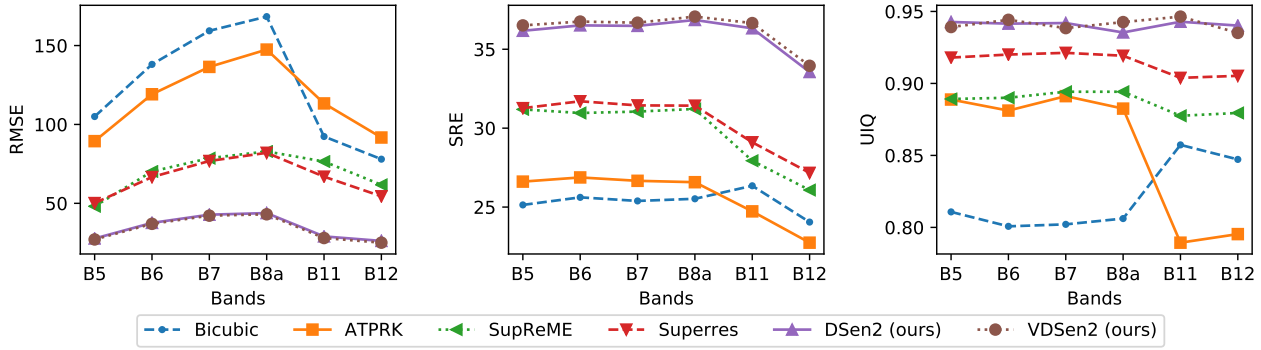


Figure 7: Per-band error metrics for 2× upsampling.

Table 4: Per-band values of RMSE, SRE and UIQ, for 2× upsampling. Values are averages over all test images. Evaluation at lower scale (input 40 m, output 20 m). Best results in bold.

| | B5 | B6 | B7 | B8a | B11 | B12 |
|---------------|--------------|--------------|--------------|--------------|--------------|--------------|
| RMSE | | | | | | |
| Bicubic | 105.0 | 138.1 | 159.3 | 168.3 | 92.4 | 78.0 |
| ATPRK | 89.4 | 119.1 | 136.5 | 147.4 | 113.3 | 91.7 |
| SupReME | 48.1 | 70.2 | 78.6 | 82.9 | 76.5 | 61.7 |
| Superres | 50.2 | 66.6 | 76.8 | 82.0 | 66.9 | 54.5 |
| DSen2 | 27.7 | 37.6 | 42.8 | 43.8 | 29.0 | 26.2 |
| VDSen2 | 27.1 | 37.0 | 42.2 | 43.0 | 28.0 | 25.1 |
| SRE | | | | | | |
| Bicubic | 25.1 | 25.6 | 25.4 | 25.5 | 26.3 | 24.0 |
| ATPRK | 26.6 | 26.9 | 26.7 | 26.6 | 24.7 | 22.7 |
| SupReME | 31.2 | 31.0 | 31.0 | 31.2 | 27.9 | 26.1 |
| Superres | 31.3 | 31.7 | 31.4 | 31.4 | 29.1 | 27.2 |
| DSen2 | 36.2 | 36.5 | 36.5 | 36.9 | 36.3 | 33.6 |
| VDSen2 | 36.5 | 36.8 | 36.7 | 37.1 | 36.7 | 34.0 |
| UIQ | | | | | | |
| Bicubic | 0.811 | 0.801 | 0.802 | 0.806 | 0.857 | 0.847 |
| ATPRK | 0.889 | 0.881 | 0.891 | 0.883 | 0.789 | 0.795 |
| SupReME | 0.889 | 0.890 | 0.894 | 0.894 | 0.878 | 0.879 |
| Superres | 0.918 | 0.920 | 0.921 | 0.919 | 0.904 | 0.905 |
| DSen2 (ours) | 0.943 | 0.942 | 0.942 | 0.935 | 0.943 | 0.940 |
| VDSen2 (ours) | 0.939 | 0.944 | 0.938 | 0.943 | 0.946 | 0.935 |

works reconstruct B11 as well as other bands and show only a slight drop in relative accuracy for B12. These two bands lie in the SWIR ($>1.6\mu\text{m}$) spectrum, far outside the spectral range covered by the high-resolution bands (0.4–0.9 μm). Especially ATPRK performs poorly on B11 and B12. The issue is further discussed in Sec. 5.5.

In Fig. 8, we compare reconstructed images to ground truth for one of the test images. Yellow denotes high residual errors, dark blue means zero error. For bands B6, B7, B8a and B11 all baselines exhibit errors along high-contrast edges (the residual images resemble a high-pass

filtering), meaning that they either blur edges or exaggerate the contrast. Our method shows only traces of this common behaviour, and has visibly lower residuals in all spectral bands.

$S_{6\times} - 60\text{ m bands}$. For 6× super-resolution we train a separate network, using synthetically downgraded images with 60 m GSD as ground truth. The baselines are run with the same settings as before (*i.e.*, jointly super-resolving all input bands) but only the 60 m bands $C = \{\text{B1}, \text{B9}\}$ are displayed. Overall and per-band results are given in

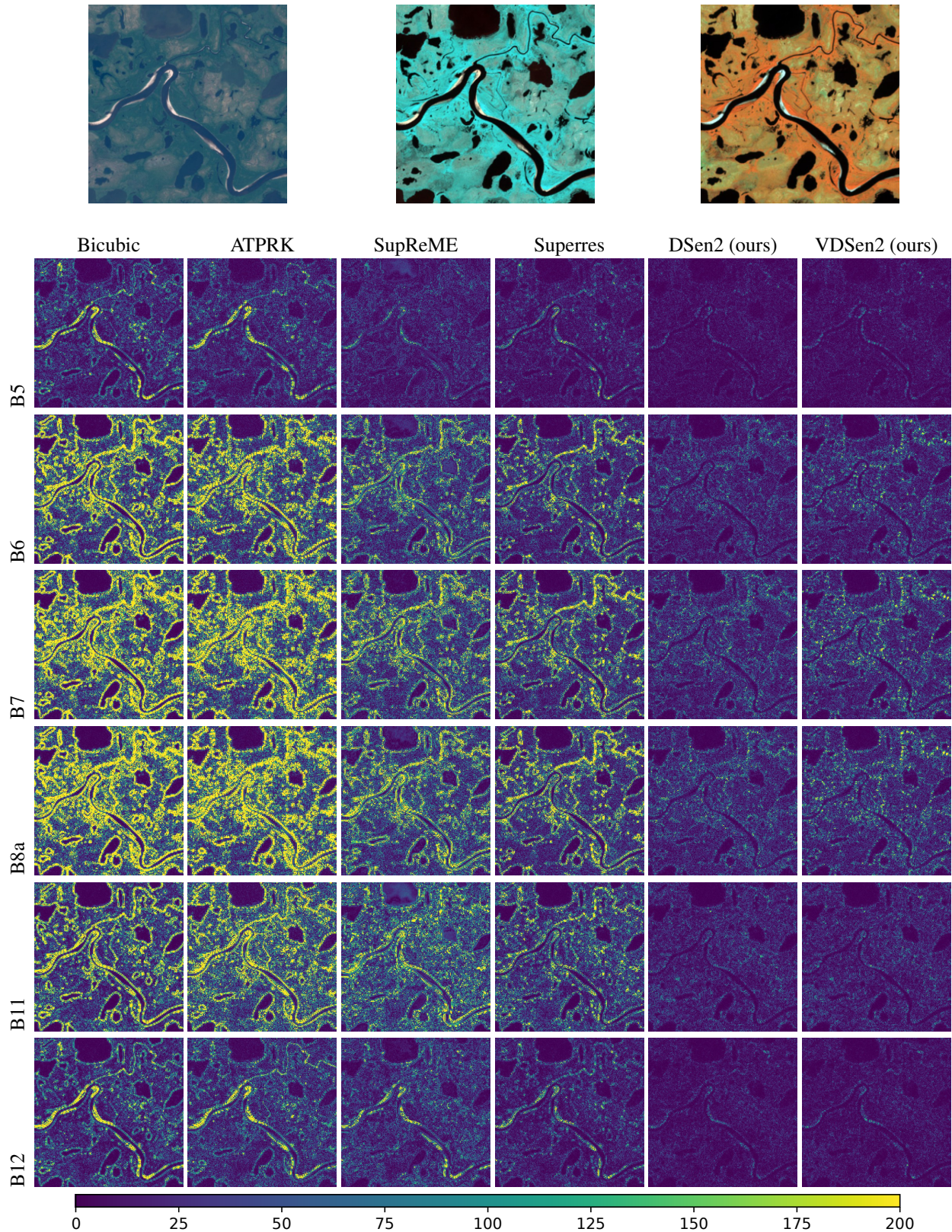


Figure 8: Absolute differences between ground truth and $2\times$ upsampled result at 20m GSD. The images show (absolute) reflectance differences on a reflectance scale from 0 to 10,000. Top, left to right: RGB (B2, B3, B4) image, color composites of bands (B5, B6, B7), and of bands (B8a, B11, B12). The image depicts the Siberian tundra near the mouth of the Pur River.

Table 5: Full results and detailed RMSE, SRE and UIQ values per spectral band. The results are averaged over all images for the $6\times$ upsampling, with evaluation at lower scale (input 360 m, output 60 m). Best results in bold.

| | B1 | | | B9 | | | Average | | | SAM |
|----------|-------------|-------------|--------------|-------------|-------------|--------------|-------------|-------------|--------------|-------------|
| | RMSE | SRE | UIQ | RMSE | SRE | UIQ | RMSE | SRE | UIQ | |
| Bicubic | 171.8 | 22.3 | 0.404 | 148.7 | 17.1 | 0.368 | 160.2 | 19.7 | 0.386 | 1.79 |
| ATPRK | 162.9 | 22.8 | 0.745 | 127.4 | 18.0 | 0.711 | 145.1 | 20.4 | 0.728 | 1.62 |
| SupReME | 114.9 | 25.2 | 0.667 | 56.4 | 24.5 | 0.819 | 85.7 | 24.8 | 0.743 | 0.98 |
| Superres | 107.5 | 24.8 | 0.566 | 92.9 | 20.8 | 0.657 | 100.2 | 22.8 | 0.612 | 1.42 |
| DSen2 | 33.6 | 35.6 | 0.912 | 30.9 | 29.9 | 0.886 | 32.2 | 32.8 | 0.899 | 0.41 |
| VDSen2 | 27.6 | 37.9 | 0.921 | 24.4 | 32.3 | 0.899 | 26.0 | 35.1 | 0.910 | 0.34 |

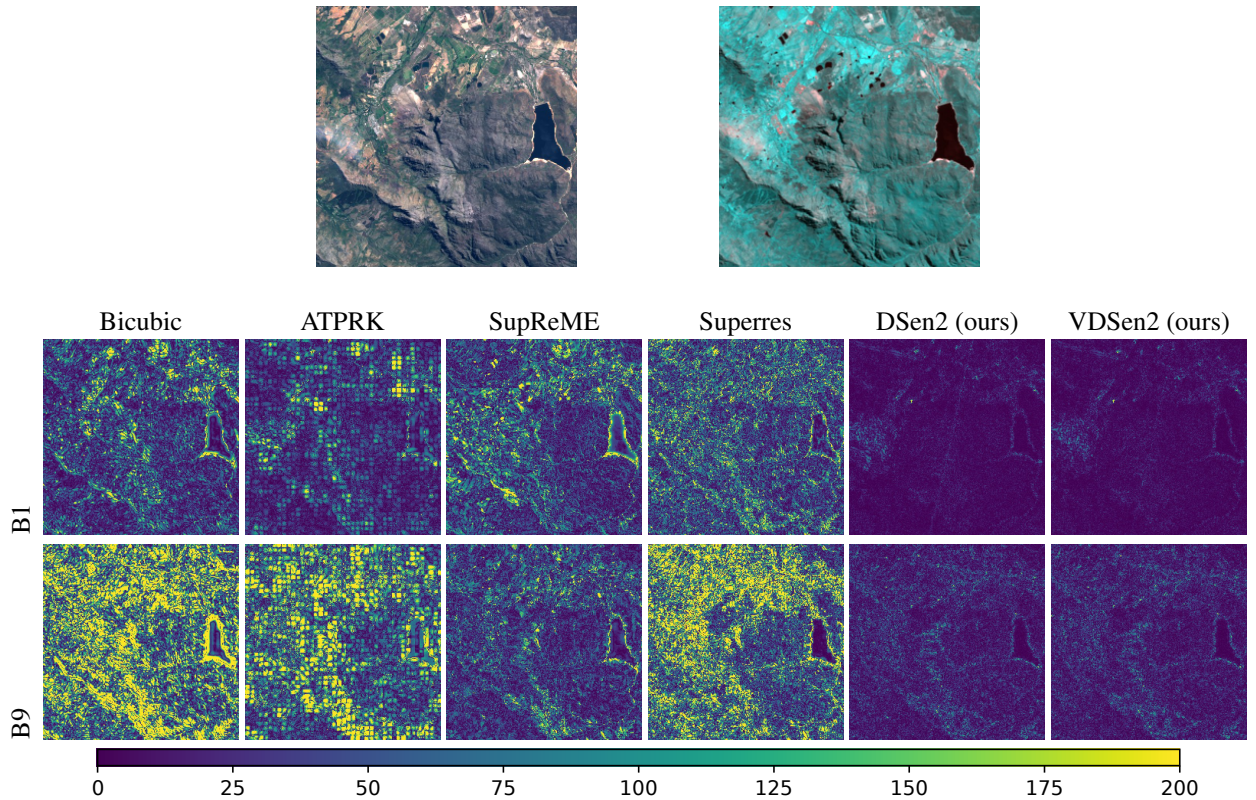


Figure 9: Absolute differences between ground truth and $6\times$ upsampled result at 60 m GSD. The images show (absolute) reflectance differences on a reflectance scale from 0 to 10,000. Top: True scene RGB (B2, B3, B4), and false color composite of B1 and B9. This image depicts Berg River Dam in the rocky Hotentots Holland, east of Cape Town, South Africa.

Table 5. Once again, our DSen2 network outperforms the previous state-of-the-art by a large margin, reducing the RMSE by a factor of ≈ 3 . For the larger upsampling factor, the very deep VDSen2 beats the shallower DSen2 by a solid margin, reaching about 20% lower RMSE, respectively 2.3 dB higher SRE.

Among the baselines, SupReME this time exhibits better overall numbers than Superres, thanks to it clearly superior performance on the B9 band. Contrary to the $2\times$ super-resolution, all baselines improve SAM compared to simple bicubic interpolation. Our method again is the runaway winner, with VDSen2 reaching 65% lower error than the nearest competitor SupReME. Looking at the individual

bands, all methods perform better (relative to average radiance) on B1 than on B9. The latter is the most challenging band for super-resolution, and the only one for which our SRE drops below 33 dB, and our UIQ below 0.9. It is worth noticing, that in this more challenging $6\times$ super-resolution, our method brings a bigger improvement compared to the state-of-the-art baselines in $2\times$ super-resolution.

We also present a qualitative comparison to ground truth, again plotting absolute residuals in Fig. 9. As for 20 m, the visual impression confirms that DSen2 and VDSen2 clearly dominate the competition, with much lower and less structured residuals.



Figure 10: Results of DSen2 on real Sentinel-2 data, for $2\times$ upsampling. From left to right: True scene RGB in 10 m GSD (B2, B3, B4), Initial 20 m bands, Super-resolved bands (B12, B8a and B5 as RGB) to 10 m GSD with DSen2. Top: An agricultural area close to Malmö in Sweden. Middle: A coastal area at the Shark Bay, Australia. Bottom: Central Park at Manhattan, New York, USA. Best viewed on computer screen.

5.4. Evaluation at the original scale

To verify that our method can be applied to true scale Sentinel-2 data, we super-resolve the same test images as before, but feed the original images, without synthetic downsampling, to our networks. As said before, we see no way to obtain ground truth data for a quantitative comparison, and therefore have to rely on visual inspection. We plot the upsampled results next to the low-resolution inputs, in Fig. 10 for $2\times$ upsampling and in Fig. 11 for $6\times$ upsampling. For each upsampling rate, the figures show 3 different test locations with varying land cover. Since visualisation is limited to 3 bands at a time, we pick bands

(B5, B8a, B12) for $2\times$ upsampling. For $6\times$ upsampling we show both bands (B1, B9). In all cases the super-resolved image is clearly sharper and brings out additional details compared to the respective input bands. At least visually, the perceptual quality of the super-resolved images matches that of the RGB bands, which have native 10 m resolution.

5.5. Suitability of pan-sharpening methods

As discussed earlier, there is a conceptual difference between multi-spectral super-resolution and classical pan-sharpening, in that the latter simply “copies” high-frequency information from an overlapping or nearby high-

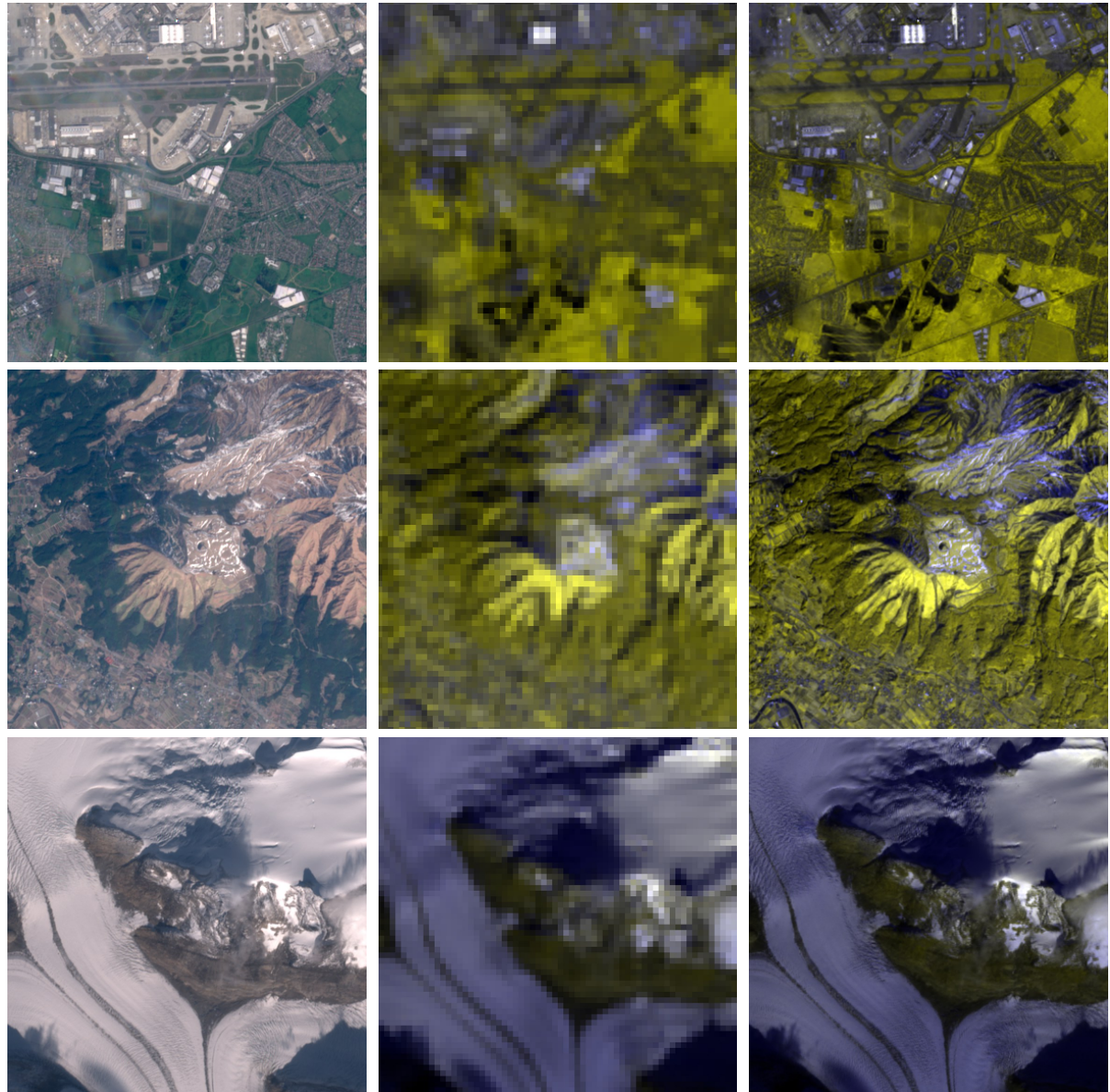


Figure 11: Results of DSen2 on real Sentinel-2 data, for $6 \times$ upsampling. From left to right: True scene RGB (B2, B3, B4), Initial 60 m bands, Super-resolved bands (B9, B9 and B1 as RGB) with DSen2. Top: London Heathrow airport and surroundings. Middle: The foot of Mt. Aso, on Kyushu island, Japan. Bottom: A glacier in Greenland. Best viewed on computer screen.

Table 6: Results of well-known pan-sharpening methods. RMSE, SRE and UIQ values per spectral band averaged over all images for the $2\times$ upsampling, with evaluation at lower scale (input 40 m, output 20 m). Best results in bold.

| | B5 | B6 | B7 | B8a | B11 | B12 | Average |
|----------------|--------------|--------------|--------------|--------------|--------------|--------------|--------------|
| RMSE | | | | | | | |
| Bicubic | 105.0 | 138.1 | 159.3 | 168.3 | 92.4 | 78.0 | 123.5 |
| PRACS | 99.3 | 148.1 | 99.2 | 104.2 | 290.0 | 320.0 | 176.8 |
| MTF-GLP-HPM-PP | 91.0 | 66.5 | 77.6 | 82.7 | 78.7 | 240.6 | 106.2 |
| BDSD | 64.7 | 84.2 | 76.0 | 78.8 | 93.4 | 79.4 | 79.4 |
| SRE | | | | | | | |
| Bicubic | 25.1 | 25.6 | 25.4 | 25.5 | 26.3 | 24.0 | 25.3 |
| PRACS | 24.0 | 24.2 | 28.7 | 29.0 | 19.5 | 14.4 | 23.3 |
| MTF-GLP-HPM-PP | 28.0 | 30.7 | 30.5 | 30.7 | 28.0 | 23.0 | 28.5 |
| BDSD | 28.3 | 29.2 | 31.1 | 31.5 | 26.3 | 23.9 | 28.4 |
| UIQ | | | | | | | |
| Bicubic | 0.811 | 0.801 | 0.802 | 0.806 | 0.857 | 0.847 | 0.821 |
| PRACS | 0.836 | 0.858 | 0.882 | 0.881 | 0.791 | 0.773 | 0.837 |
| MTF-GLP-HPM-PP | 0.893 | 0.898 | 0.909 | 0.909 | 0.877 | 0.881 | 0.895 |
| BDSD | 0.866 | 0.892 | 0.909 | 0.908 | 0.858 | 0.848 | 0.880 |

resolution band, but cannot exploit the overall reflectance distribution across the spectrum. Still, it is a-priori not clear how much of a practical impact this has, therefore we also test three of the best-performing pan-sharpening methods in the literature, namely PRACS (Choi et al., 2011), MTF-GLP-HPM-PP (Lee and Lee, 2010) and BDSD (Garzelli et al., 2008). Quantitative error measures for the $2\times$ case are given in Table 6. Pan-sharpening requires a single “panchromatic” band as high-resolution input. The combinations that empirically worked best for our data were the following: For the near-infrared bands B6, B7 and B8a, we use the broad high-resolution NIR band B8. As panchromatic band for B5 we use B2, which surprisingly worked better than the spectrally closer B8, and also slightly better than other visual bands. While for the SWIR bands there is no spectrally close high-resolution band, and the best compromise appears to be the average of the three visible bands, $\frac{1}{3}(B2+B3+B4)$.

For bands B5, B6, B7 and B8 the results are reasonable: the errors are higher than those of the best super-resolution baseline (and consequently 2-3× higher than with our networks, *c.f.* Table 4), but lower than naive bicubic upsampling. This confirms that there is a benefit from using all bands together, rather than the high-frequency data from only one, arbitrarily defined “panchromatic” band.

On the contrary, for the SWIR bands B11 and B12 the performance of pan-sharpening drops significantly, to a point that the RMSE drops below that of bicubic interpolation (and similar for SRE). As was to be expected, successful pan-sharpening is not possible with a spectrally distant band that has very different image statistics and local appearance. Moreover, pan-sharpening is very sensitive to

the choice of the “panchromatic” band. We empirically picked the one that worked best on average, but found that, for all tested methods, there isn’t one that performs consistently across all test images. This is particularly evident for MTF-GLP-HPM-PP. Even with the best pan-band we found (the average of the visible bands), it reconstructed reasonable SWIR bands for some images, but completely failed on others, leading to excessive residuals.⁴

While it may be possible to improve pan-sharpening performance with some sophisticated, perhaps non-linear combination for the pan-band, determining that combination is a research problem on its own, and beyond the scope of this paper.

For readability, the pan-sharpening results are displayed in a separate table. We note for completeness that, among the super-resolution baselines (Tables 3 and 4), ATPRK is technically also a pan-sharpening method, but includes a mechanism to automatically select one of several high-resolution channels as its the “panchromatic” input. We categorise it as super-resolution, since its creators also intend and apply it for that purpose. It can be seen in Table 4 that ATPRK actually also exhibits a distinct performance drop for bands B11 and B12.

Overall, we conclude that pan-sharpening cannot substitute qualified super-resolution, and is not suitable for Sentinel-2. Nevertheless, we point out that in the literature, the difficulties it has especially with bands B11 and B12 is sometimes masked, because many papers do not show the

⁴ Actually, for MTF-GLP-HPM-PP we had to exclude one of the 15 images from the evaluation, since the method did not produce a valid output.

individual per-band errors.

6. Discussion

6.1. Different network configurations

The behaviour of our two tested network configurations is in line with the recent literature: networks of moderate size (by today’s standards), like DSen2, already perform fairly well. Across a wide range of image analysis tasks from denoising to instance-level semantic segmentation and beyond, CNNs with around 10–20 layers have redefined the state-of-the-art. Over the last few years, improvements to the network architecture have enabled training of very deep networks with even more (in some cases >100) layers, like VDSen2. Empirically, these models tend to raise the bar even further, but the gains are less dramatic, as adding more and more layers faces diminishing returns. Somewhat surprisingly, even the very deep models with tens of millions of free parameters do not show a strong tendency to overfit, if designed correctly. We note that our networks differ from the prevalent design for high-level analysis (semantic segmentation, depth estimation, etc.). These normally have an “hourglass” structure with an encoder part that successively increases the receptive field (respectively, reduces the spatial resolution) via pooling operations, followed by a decoder part that restores the original resolution via transposed convolutions. We refrain from pooling, since it carries the danger of degrading local detail, while conversely a fairly small neighbourhood is, in our view, sufficient to determine the local spectral relations.

What is the “right” depth for super-resolution? As usual in such cases, there is no single answer, since this depends on the specific application (*e.g.*, variability of the land-cover, available computational resources, update frequency, *etc.*). As a general guideline, we find that, with adequate hardware at hand, there is no disadvantage in using VDSen2. It is neither more difficult to use nor more brittle to train from the perspective of the user. While it does consistently produce super-resolved images with lower residuals, especially for the challenging $6\times$ upsampling. If hardware resources (especially GPU memory) are limited, or very large interest regions must be processed in a short time, it may nevertheless be better to work with DSen2. The results are still very good, and in certain cases, *e.g.*, if only $2\times$ upsampling is needed and/or the spectral variability in the interest region is not too high will probably match the performance of a deeper architecture. Importantly, intermediate variants are also possible: if one aims for the highest possible quality under limited resources, it may make sense to chose a number of ResBlocks between the $d = 6$ of DSen2 and the $d = 32$ of VDSen2. In fact, for “easy” land-cover or if maximal accuracy is not needed (*e.g.*, for visualisation) it may well be possible to remove another 1 or 2 ResBlocks from DSen2 and still obtain satisfactory results.

Table 7: Runtimes for super-resolving the six 20 m bands of a standard Sentinel-2 tile (10980×10980 pixels, ≈ 120 Mpix).

| Method | CPU time | GPU time |
|---------------|----------------|----------|
| Bicubic | $\ll 1$ min | — |
| ATPRK | 149 min | — |
| SupReME | 123 min | — |
| Superres | 315 min | — |
| DSen2 (ours) | 130 min | 3 min |
| VDSen2 (ours) | ≈ 30 h | 14 min |

6.2. Timing

As in general for deep learning, training a network is computationally demanding and takes time (often several days, see sec. 4.5), but the single forward pass to super-resolve a new image is very fast. We note that long training times are usually required only once, when training from scratch. Refining/adapting an existing network with further training data is a lot less costly. Our pretrained networks can serve as a starting point.

In Table 7 the runtimes of all tested methods are presented for super-resolving all 20 m bands of a complete Sentinel-2 tile ($10,980 \times 10,980$ pixels). The baselines are only available as CPU code, and in some cases not easy to parallelise, whereas CNNs are almost always run on GPUs – in fact, their current revival was, to a large part, triggered by the advent of parallel computing on GPUs. We therefore show both processing times. The comparison is indicative and not meant to claim our method is a lot faster than the baselines: modern CNN frameworks are highly optimised, whereas the baselines are research implementations with much potential for speed-ups. Still, the numbers are useful to show that CNN-based super-resolution is fairly efficient, and clearly fast enough to be used in practice without much further code optimisation. For the Comparison, we used an Intel(R) Xeon(R) CPU E5-1650 v3 @ 3.50GHz, respectively an NVIDIA Titan Xp GPU. On a desktop computer with a single GPU, DSen2 super-resolves a complete Sentinel-2 tile to 10 m in 3 minutes, and VDSen2 in 14 minutes. We note that hardware producers are working on specialised tensor processing hardware that is optimised for deep learning (rather than gaming and computer graphics), and can be expected to further speed up CNNs. We do point out that if no powerful GPU is available, very deep networks are not viable. On the contrary, DSen2 takes ≈ 2 hours of CPU time and is comparable with the fastest baseline method.

6.3. Open-source publication of our models

The publication of this paper includes open, publicly available implementations of our models, at: <https://github.com/lanha/DSen2>. We provide the python source files (in Keras format) for the network specifications as well as the training procedure. Moreover, we also

provide the already trained weights used in all our experiments. These shall enable out-of-the-box super-resolution of Sentinel-2 images world-wide, with minimal knowledge of neural network tools. Of course, if a study is focussed only in a specific geographic location, biome or land-cover type, even better result can be expected by training the network only with images showing those specific conditions. The literature suggests that in that case, it may be best to start from our globally trained network and fine-tune it through further training iterations on task-specific imagery.

In the future, we hope to also integrate our method into the SNAP toolbox for Sentinel-2 processing, so as to use our super-resolution instead of naive upsampling within the processing pipeline. A word of caution: our weights are trained only on real Sentinel-2 images, and their excellent performance is to a large part due to the fact that they are optimised specifically for the image statistics of the input data. They are therefore not suitable for processing data from other sensors, or other processing levels of Sentinel-2.

7. Conclusions

We have described a tool to super-resolve (“sharpen”) the lower-resolution (20 m and 60 m) bands of Sentinel-2 to a uniform 10 m GSD data cube. Our method uses two deep convolutional neural networks to jointly learn the mapping from all input bands to the 2 \times , respectively 6 \times super-resolved output bands. To train the network, we make the empirically plausible assumption that the correct way of transferring high-frequency information across spectral bands is invariant over a range of scales. In this way, we can synthesise arbitrary amounts of training data with known ground truth from the Sentinel-2 archive. We sample a large and varied global dataset that, according to our experiments, yields a super-resolution tool that generalises to unseen locations in different parts of the world.

The super-resolution network shows excellent performance, reducing the RMSE of the prediction by 50% compared to the best competing methods; respectively, increasing the SRE by almost 6 dB. Qualitative results from different land-cover types, biomes and climate zones confirm the good performance also on full-resolution S2 images. Moreover, the method is also fast enough for practical large-scale applications, computation times are on the order of a few minutes for a complete, 120 MPix Sentinel-2 tile.

While in our work we have focussed on Sentinel-2, the networks are learned end-to-end from image data and thus completely generic. We are confident that they can be retrained for super-resolution of different multi-resolution multi-spectral sensors. We make our software and models available as open-source tools for the remote sensing community.

Acknowledgments

The authors acknowledge financial support from the Swiss National Science Foundation (SNSF), project No. 200021_162998, Fundação para a Ciência e a Tecnologia, Portuguese Ministry of Science, Technology and Higher Education, projects UID/EEA/50008/2013 and ER-ANETMED/0001/2014.

References

- Brodu, N., Aug 2017. Super-resolving multiresolution images with band-independent geometry of multispectral pixels. *IEEE Transactions on Geoscience and Remote Sensing* 55 (8), 4610–4617.
- Castillo, J. A. A., Apan, A. A., Maraseni, T. N., Salmo III, S. G., 2017. Estimation and mapping of above-ground biomass of mangrove forests and their replacement land uses in the philippines using Sentinel imagery. *ISPRS Journal of Photogrammetry and Remote Sensing* 134, 70 – 85.
- Choi, J., Yu, K., Kim, Y., 2011. A new adaptive component-substitution-based satellite image fusion by using partial replacement. *IEEE Transactions on Geoscience and Remote Sensing* 49 (1), 295–309.
- Chollet, F., et al., 2015. Keras. <https://github.com/fchollet/keras>.
- Clerc, S., MPC Team, 2018. S2 MPC - Data Quality Report. ESA, reference S2-PDGS-MPC-DQR, issue 23. [Online: <http://earth.esa.int/documents/247904/685211/Sentinel-2-Data-Quality-Report>, accessed 01 Feb. 2018].
- Clevers, J., Kooistra, L., Van Den Brande, M., 2017. Using sentinel-2 data for retrieving lai and leaf and canopy chlorophyll content of a potato crop. *Remote Sensing* 9 (5), 405.
- Deloye, C., Weiss, M., Defourny, P., 2018. Retrieval of the canopy chlorophyll content from sentinel-2 spectral bands to estimate nitrogen uptake in intensive winter wheat cropping systems. *Remote Sensing of Environment* 216, 245–261.
- Dozat, T., 2015. Incorporating Nesterov momentum into Adam. Tech. rep., Stanford University, Tech. Rep. [Online: http://cs229.stanford.edu/proj2015/054_report.pdf, accessed 06 Feb. 2018].
- Du, Y., Zhang, Y., Ling, F., Wang, Q., Li, W., Li, X., 2016. Water bodies mapping from Sentinel-2 imagery with modified normalized difference water index at 10-m spatial resolution produced by sharpening the SWIR band. *Remote Sensing* 8 (4), 354.
- Fasbender, D., Tuia, D., Bogaert, P., Kanevski, M., 2008. Support-based implementation of Bayesian data fusion for spatial enhancement: Applications to ASTER thermal images. *IEEE Geoscience and Remote Sensing Letters* 5 (4), 598–602.
- Freeman, W. T., Jones, T. R., Pasztor, E. C., 2002. Example-based super-resolution. *IEEE Computer graphics and Applications* 22 (2), 56–65.
- Garzelli, A., Nencini, F., Capobianco, L., 2008. Optimal mmse pan sharpening of very high resolution multispectral images. *IEEE Transactions on Geoscience and Remote Sensing* 46 (1), 228–236.
- Gasparovic, M., Jogun, T., 2018. The effect of fusing Sentinel-2 bands on land-cover classification. *International Journal of Remote Sensing* 39 (3), 822–841.
- Glasner, D., Bagon, S., Irani, M., 2009. Super-resolution from a single image. In: *IEEE International Conference on Computer Vision*. pp. 349–356.
- He, K., Zhang, X., Ren, S., Sun, J., 2015. Delving deep into rectifiers: Surpassing human-level performance on imagenet classification. In: *IEEE Conference on Computer Vision and Pattern Recognition (CVPR)*. pp. 1026–1034.
- He, K., Zhang, X., Ren, S., Sun, J., 2016. Deep residual learning for image recognition. In: *IEEE Conference on Computer Vision and Pattern Recognition (CVPR)*. pp. 770–778.

- Huang, G., Liu, Z., van der Maaten, L., Weinberger, K. Q., 2017. Densely connected convolutional networks. In: IEEE Conference on Computer Vision and Pattern Recognition (CVPR). pp. 2261–2269.
- Immitzer, M., Vuolo, F., Atzberger, C., 2016. First experience with Sentinel-2 data for crop and tree species classifications in central Europe. *Remote Sensing* 8 (3), 166.
- Kim, J., Kwon Lee, J., Mu Lee, K., 2016. Accurate image super-resolution using very deep convolutional networks. In: IEEE Conference on Computer Vision and Pattern Recognition (CVPR). pp. 1646–1654.
- Kingma, D., Ba, J., 2014. Adam: A method for stochastic optimization. arXiv preprint arXiv:1412.6980.
- Lanaras, C., Bioucas-Dias, J., Baltasavias, E., Schindler, K., 2017. Super-resolution of multispectral multiresolution images from a single sensor. In: IEEE Conference on Computer Vision and Pattern Recognition Workshops (CVPRW). pp. 1505–1513.
- Lee, J., Lee, C., 2010. Fast and efficient panchromatic sharpening. *IEEE Transactions on Geoscience and Remote Sensing* 48 (1), 155–163.
- Lim, B., Son, S., Kim, H., Nah, S., Lee, K. M., 2017. Enhanced deep residual networks for single image super-resolution. In: IEEE Conference on Computer Vision and Pattern Recognition Workshops (CVPRW). pp. 1132–1140.
- Masi, G., Cozzolino, D., Verdoliva, L., Scarpa, G., 2016. Pansharpening by convolutional neural networks. *Remote Sensing* 8 (7), 594.
- Mura, M., Bottalico, F., Giannetti, F., Bertani, R., Giannini, R., Mancini, M., Orlandini, S., Travaglini, D., Chirici, G., 2018. Exploiting the capabilities of the Sentinel-2 multi spectral instrument for predicting growing stock volume in forest ecosystems. *International Journal of Applied Earth Observation and Geoinformation* 66, 126 – 134.
- Paris, C., Bioucas-Dias, J., Bruzzone, L., July 2017. A hierarchical approach to superresolution of multispectral images with different spatial resolutions. In: IEEE International Geoscience and Remote Sensing Symposium (IGARSS). pp. 2589–2592.
- Park, H., Choi, J., Park, N., Choi, S., 2017. Sharpening the VNIR and SWIR bands of Sentinel-2A imagery through modified selected and synthesized band schemes. *Remote Sensing* 9 (10), 1080.
- Paul, F., Winsvold, S. H., Kb, A., Nagler, T., Schwaizer, G., 2016. Glacier remote sensing using Sentinel-2. Part II: Mapping glacier extents and surface facies, and comparison to Landsat 8. *Remote Sensing* 8 (7).
- Pesaresi, M., Corbane, C., Julea, A., Florczyk, A. J., Syrris, V., Soille, P., 2016. Assessment of the added-value of Sentinel-2 for detecting built-up areas. *Remote Sensing* 8 (4), 299.
- Picaro, G., Addesso, P., Restaino, R., Vivone, G., Picone, D., Dalla Mura, M., 2016. Thermal sharpening of VIIRS data. In: IEEE International Geoscience and Remote Sensing Symposium (IGARSS). pp. 7260–7263.
- Pouliot, D., Latifovic, R., Pasher, J., Duffe, J., 2018. Landsat super-resolution enhancement using convolution neural networks and Sentinel-2 for training. *Remote Sensing* 10 (3), 394.
- Ruderman, D. L., 1994. The statistics of natural images. *Network: Computation in Neural Systems* 5 (4), 517–548.
- Scarpa, G., Vitale, S., Cozzolino, D., 2018. Target-adaptive cnn-based pansharpening. *IEEE Transactions on Geoscience and Remote Sensing* (99), 1–15.
- Shechtman, E., Irani, M., 2007. Matching local self-similarities across images and videos. In: IEEE Conference on Computer Vision and Pattern Recognition (CVPR).
- Simonyan, K., Zisserman, A., 2015. Very deep convolutional networks for large-scale image recognition. In: International Conference on Learning Representations.
- Sirguey, P., Mathieu, R., Arnaud, Y., Khan, M. M., Chanussot, J., 2008. Improving MODIS spatial resolution for snow mapping using wavelet fusion and ARSIS concept. *IEEE Geoscience and Remote Sensing Letters* 5 (1), 78–82.
- Srivastava, A., Lee, A. B., Simoncelli, E. P., Zhu, S.-C., 2003. On advances in statistical modeling of natural images. *Journal of Mathematical Imaging and Vision* 18 (1), 17–33.
- Szegedy, C., Ioffe, S., Vanhoucke, V., Alemi, A. A., 2017. Inception-v4, inception-resnet and the impact of residual connections on learning. In: Proceedings of the Thirty-First AAAI Conference on Artificial Intelligence (AAAI-17).
- Toming, K., Kutser, T., Laas, A., Sepp, M., Paavel, B., Ngess, T., 2016. First experiences in mapping lake water quality parameters with Sentinel-2 MSI imagery. *Remote Sensing* 8 (8), 640.
- Tonooka, H., 2005. Resolution enhancement of ASTER shortwave and thermal infrared bands based on spectral similarity. In: Proc. SPIE. Vol. 5657. pp. 9–19.
- Trishchenko, A. P., Luo, Y., Khlopenkov, K. V., 2006. A method for downscaling MODIS land channels to 250-m spatial resolution using adaptive regression and normalization. In: Proc. SPIE. Vol. 6366. pp. 636607–636607–8.
- Vaiopoulos, A., Karantzalos, K., 2016. Pansharpening on the narrow VNIR and SWIR spectral bands of Sentinel-2. *ISPRS-International Archives of the Photogrammetry, Remote Sensing and Spatial Information Sciences* XLI-B7, 723–730.
- van der Schaaf, A., van Hateren, J. H., 1996. Modelling the power spectra of natural images: Statistics and information. *Vision Research* 36 (17), 2759–2770.
- Vivone, G., Alparone, L., Chanussot, J., Dalla Mura, M., Garzelli, A., Licciardi, G. A., Restaino, R., Wald, L., 2015. A critical comparison among pansharpening algorithms. *IEEE Transactions on Geoscience and Remote Sensing* 53 (5), 2565–2586.
- Wang, Q., Shi, W., Li, Z., Atkinson, P. M., 2016. Fusion of Sentinel-2 images. *Remote Sensing of Environment* 187, 241–252.
- Wang, Z., Bovik, A. C., March 2002. A universal image quality index. *IEEE Signal Processing Letters* 9 (3), 81–84.
- Yang, J., Fu, X., Hu, Y., Huang, Y., Ding, X., Paisley, J., 2017. Pannet: A deep network architecture for pan-sharpening. In: IEEE Conference on Computer Vision and Pattern Recognition (CVPR). pp. 5449–5457.
- Yuhas, R. H., Goetz, A. F., Boardman, J. W., 1992. Discrimination among semi-arid landscape endmembers using the spectral angle mapper (SAM) algorithm. In: Summaries of the Third Annual JPL Airborne Geoscience Workshop. Vol. 1. pp. 147–149.